Broadband synthetic aperture geoacoustic inversion

Bien Aik Tan,[a] Peter Gerstoft, Caglar Yardim, and William S. Hodgkiss
Marine Physical Laboratory, Scripps Institution of Oceanography, University of California San Diego, 9500 Gilman Drive, La Jolla, California 92093-0238

(Received 22 December 2012; revised 24 April 2013; accepted 29 April 2013)

A typical geoacoustic inversion procedure involves powerful source transmissions received on a large-aperture receiver array. A more practical approach is to use a single moving source and/or receiver in a low signal to noise ratio (SNR) setting. This paper uses single-receiver, broadband, frequency coherent matched-field inversion and exploits coherently repeated transmissions to improve estimation of the geoacoustic parameters. The long observation time creates a synthetic aperture due to relative source-receiver motion. This approach is illustrated by studying the transmission of multiple linear frequency modulated (LFM) pulses which results in a multi-tonal comb spectrum that is Doppler sensitive. To correlate well with the measured field across a receiver trajectory and to incorporate transmission from a source trajectory, waveguide Doppler and normal mode theory is applied. The method is demonstrated with low SNR, 100–900 Hz LFM pulse data from the Shallow Water 2006 experiment. © *2013 Acoustical Society of America*. [http://dx.doi.org/10.1121/1.4807567]

PACS number(s): 43.60.Pt [ZHM] Pages: 312–322

I. INTRODUCTION

Typically, matched-field inversion experiments use large-aperture arrays and powerful transmissions with high SNR. However, single-receiver/synthetic aperture inversion methods are preferable operationally due to ease of deployment.[1–14] Furthermore, low SNR methods are attractive due to their ability to use low powered sources, e.g., battery powered acoustic sources,[15] resulting in less disturbance to marine mammals.[4] This paper focuses on matched field inversion for mobile, single source-receiver configurations in low SNR conditions.

Four main types of single-receiver/synthetic aperture based geoacoustic inversion/source localization methods have been proposed: (1) dispersion curve analysis,[1–4] (2) the matched impulse response method,[5–10] (3) matched field processing,[11,12] and (4) synthetic aperture modal inverse techniques.[13,14]

Ship noise is a good source of opportunity for carrying out inversions. Using relative dispersion curves combined with waveguide invariant principles, ship noise data is inverted for a simple Pekeris waveguide in Ref. 4 using just one receiver with a few dB SNR. Other dispersion based inversions[1–3] are done using imploding glass bulbs or air guns (impulsive sources). These methods work well only for low frequency sources ($f < 200$ Hz) and use long propagation distances to separate the dispersion between the modes.

Here, a single-receiver, broadband, frequency-coherent matched-field inversion procedure is formulated to exploit coherently repeated transmissions to reduce estimation uncertainty without resorting to powerful source transmissions. Due to the repeated transmissions and longer observation time, the overall source spectrum becomes increasingly Doppler sensitive. In addition, the source-receiver relative motion also creates a longer synthetic aperture that is utilized in the inversion. To correlate well with the measured field, waveguide Doppler and normal mode theory is applied.[16–21] Similar waveguide Doppler modeling has been used in narrowband synthetic aperture modal inverse methods.[13,14,22,23] Other moving source or receiver inversion methods[4–6] mitigated Doppler effects in the received signal instead of the forward model, which may result in residual errors.

Modeling waveguide Doppler requires coupling the source spectrum to the Green's function of the medium. As a result, the source spectrum needs to be known. Assuming the source spectrum is known, the impact of exploiting coherently multiple transmissions and waveguide Doppler on single-receiver matched-field inversions is examined. The method is well suited for low SNR scenarios as well as rapid environment assessment using a horizontally moving source and receiver. The theory of waveguide Doppler and modal propagation is briefly reviewed in Sec. II, followed by the formulation of the inversion problem. Simulation results are presented in Sec. III. Section IV presents results from the analysis of experimental data.

II. THEORY

A. A review on waveguide Doppler

The Doppler effect, due to source and/or receiver motion, on a signal propagating in free space is described by a simple Galilean transformation.[24] However, in a waveguide, the Doppler effect is more complicated due to the multipath phenomenon, e.g., Refs. 16–21. In this paper, we adopt the range-independent waveguide Doppler theory derived by Schmidt and Kuperman[18,19] to synthesize the field. This implies that each horizontal wave number or mode will undergo a different Doppler shift. The scenario considered is depicted in Fig. 1.

Reasons for choosing the Schmidt and Kuperman[18,19] waveguide Doppler model are (1) it has both spectral and modal solutions which can be adapted from several commonly used acoustic models, (2) it recognizes the non-reciprocity of source and receiver motion which means that

[a]Author to whom correspondence should be addressed. Electronic mail: btan@ucsd.edu

 0001-4966/2013/134(1)/312/11/$30.00

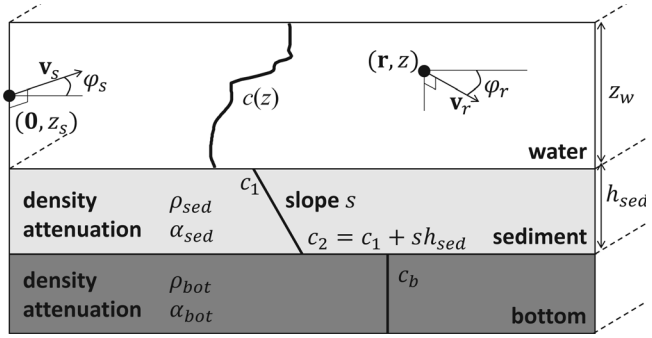

FIG. 1. Horizontally stratified ocean with horizontally moving source and receiver. The source is moving at velocity $\mathbf{v}_s$ and bearing φ_s, while the receiver is moving at velocity $\mathbf{v}_r$ and bearing φ_r. Range origin is defined as the source position at time zero when the source begins transmitting.

the Doppler is a function of source and receiver motion and not of relative motion alone, and (3) the solution is in the frequency domain thus directly applicable to frequency coherent matched field processing. However, the model only allows horizontal motion which is adequate since most moving underwater sources and receivers are horizontally towed or propelled.

1. Waveguide Doppler normal mode representation

The theory begins with the Cartesian coordinate inhomogeneous wave equation, incorporating only a moving harmonic point source with constant horizontal velocity vector $\mathbf{v}_s$ and source frequency ω_s. $S(\omega_s)$ is the source spectrum representing the amplitude and phase of the harmonic point source.

$$\nabla^2\psi(\mathbf{r}, z; t) - \frac{1}{c^2}\frac{\partial^2\psi(\mathbf{r}, z; t)}{\partial t^2} = -\delta(\mathbf{r} - \mathbf{v}_s t)\delta(z - z_s)S(\omega_s)e^{-i\omega_s t}. \quad (1)$$

Following the Fourier transform conventions and derivations in Schmidt and Kuperman,[18,19] and defining the receiver position vector, $\mathbf{r}$, as a function of horizontal receiver velocity $\mathbf{v}_r$ and time,

$$\mathbf{r} = \mathbf{r_0} + \mathbf{v}_r t, \quad (2)$$

where $\mathbf{r_0}$ is the receiver position at $t = 0$. The range-frequency domain solution for the field is

$$\psi(\mathbf{r}, z; \omega_r) = \frac{1}{2\pi}\int S[\omega_s^{(\mathbf{k})}]g(k, z; \omega_r + \mathbf{k}\cdot\mathbf{v}_r)e^{i\mathbf{k}\cdot\mathbf{r_0}}\mathrm{d}^2\mathbf{k}, \quad (3)$$

where $\mathbf{r}$ represents a straight line, Eq. (2), describing the receiver trajectory since the frequency domain solution integrates over time. g is the depth dependent Green's function at propagation frequency ω and ω_r is the receiver frequency. $k = |\mathbf{k}|$ is the horizontal wave number and the Doppler-shifted source frequency is

$$\omega_s^{(\mathbf{k})} = \omega_r - \mathbf{k}\cdot(\mathbf{v}_s - \mathbf{v}_r). \quad (4)$$

Equation (3) is exact within the theory of linear acoustics, i.e., the turbulence caused by the ambient flow across the source or receiver is negligible.[24] Therefore, it is implicit that source or receiver velocities v,

$$\text{A1} : v/c \ll 1. \quad (5)$$

Another assumption is

$$\text{A2} : \mathbf{v}_r \text{ and } \mathbf{v}_s \text{ are constants and horizontal,} \quad (6)$$

which result in the simplified field described in Eq. (3). Equation (3) is computationally intensive due to the 2-D wave number integral. The wave number integration is reduced to a single dimension by making a third assumption. This means that the radial velocities approximately are constant:

$$\text{A3} : v_r = |\mathbf{v}_r|\cos\varphi_r, \quad v_s = |\mathbf{v}_s|\cos\varphi_s. \quad (7)$$

Furthermore, by replacing the kernel with a modal Green's function,[18,19] the normal mode representation is

$$\psi(\mathbf{r}, z, \omega_r) \approx \frac{i}{4\rho(z_s)}\sum_n S[\omega_s^{(k_n)}]\,\Psi_n(z; \omega_r + k_n v_r) \times \Psi_n(z_s; \omega_r + k_n v_r)H_0^{(1)}(k_n r_0), \quad (8)$$

where

$$\omega_s^{(k_n)} = \omega_r - k_n(v_s - v_r), \quad (9)$$

$$H_0^{(1)}(k_n r_0) \approx \sqrt{\frac{2}{\pi k_n r_0}}e^{i(k_n r_0 - \pi/4)}. \quad (10)$$

K_n and Ψ_n are the modal wave numbers and modal functions evaluated at propagation frequencies ω. Table I summarizes the relationship of source, propagation, and receiver frequencies.

For numerical efficiency, constructing the field in Eq. (8) is facilitated by some approximations to the propagation modal wave numbers and functions that are computed instead from ω_r. In addition, modal cutoffs or additions introduced by Doppler are neglected:

$$\text{A4} : \Psi(z; \omega) \approx \Psi(z; \omega_r) \approx \Psi(z; \omega_s). \quad (11)$$

$$\text{A5} : \text{Modal cutoffs/additions are neglected.} \quad (12)$$

Hence, the modal functions evaluated at ω can be approximated from modal functions at ω_r. Propagation modal wave number k_n then is approximated using Taylor's approximation. For the higher order terms to be negligible, the wave number change due to the shift in propagation frequency is assumed locally linear.[18,19] This means that the frequency shift with respect to source or receiver frequency is small

TABLE I. Source, propagation, and receiver frequencies mapping relationships where the first row is with respect to receiver frequency ω_r and the second is with respect to source frequency ω_s.

Source	Propagation	Receiver
$\omega_s^{(k_n)} = \omega_r - k_n(v_s - v_r)$	$\omega = \omega_r + k_n v_r$	ω_r
ω_s	$\omega = \omega_s + k_n v_s$	$\omega_r^{(k_n)} = \omega_s + k_n(v_s - v_r)$

assuming Eq. (5). Let k_n be a function of angular frequency ω, which is $k_n = k_n(\omega)$:

$$\text{A6}: \; k_n = k_n(\omega_r + k_n v_r) \approx k_n(\omega_r) + \frac{dk_n(\omega_r)}{d\omega_r} k_n v_r \approx \frac{k_{rn}}{(1 - v_r/u_{rn})}, \tag{13}$$

where $u_{rn} = (d\omega_r)/[dk_n(\omega_r)]$ is the nth modal group velocity and $k_{rn} = k_n(\omega_r)$ is the nth modal wave number, both evaluated at ω_r. This approximation works backward from the receiver frequency. A forward k_n approximation based on ω_s also can be done using the same method in Eq. (13):

$$\text{A7}: \; k_n = k_n(\omega_s + k_n v_s) \approx \frac{k_{sn}}{(1 - v_s/u_{sn})}, \tag{14}$$

where $u_{sn} = (d\omega_s)/[dk_n(\omega_s)]$ is the nth modal group velocity and $k_{sn} = k_n(\omega_s)$ is the nth modal wave number, both evaluated at ω_s.

Substituting Eqs. (11) and (13) into Eq. (8), the Doppler shifted field via normal mode representation is obtained:

$$\psi(\mathbf{r}, z, \omega_r) \approx \frac{ie^{-i(\pi/4)}}{\sqrt{8\pi}\rho(z_s)} \sum_n S[\omega_s^{(k_n)}] \times \Psi_n(z; \omega_r)\Psi_n(z_s; \omega_r) \frac{e^{ik_n r_0}}{\sqrt{k_n r_0}}. \tag{15}$$

In the case where the wave number k_{rn} is complex to manifest absorption losses, the resulting complex propagation wave number k_n can still be approximated using Eq. (16). The steps for generating the Doppler shifted field using normal modes are summarized as follows:

(1) Compute the normal modes as per the static case evaluated at ω_r giving $\{\Psi_n(z_s; \omega_r), \Psi_n(z; \omega_r), k_{rn}, u_{rn}\}$;
(2) With u_{rn} and v_r known, compute the propagation horizontal wave number k_n using Eq. (13);
(3) Extract the source spectrum $S[\omega_r - k_n(v_s - v_r)]$ and compute $\psi(\mathbf{r}, z, \omega_r)$ using Eq. (15).

For a static field computation, $\omega_r = \omega_s$. On the other hand, with relative motion, a waveguide Doppler field computation at ω_r traces back to multiple source frequencies, see Eqs. (9) and (15). This backward mode-dependent frequency mapping is the main difference when compared to the static field computation.

B. Likelihood and cost functions

The problem of matched field inversion to infer parameters characterizing the ocean environment is nonlinear due to the nonlinear relationship between the acoustic field and the parameters. Section II B 1 describes the maximum likelihood (ML) formulations for the frequency-coherent likelihood and cost functions of a single receiver in additive colored noise.

1. Frequency-coherent likelihood and cost functions of a moving source and receiver

A broadband data model for frequency-coherent matched-field based geoacoustic inversion has been proposed.[25–27] Here, this model is improved by including source/receiver motion and realistic noise assumptions,

$$\mathbf{y} = \alpha \mathbf{E}(\xi)\mathbf{d}(\mathbf{m}) + \mathbf{w} = \alpha \mathbf{b}(\xi, \mathbf{m}) + \mathbf{w}, \tag{16}$$

where $\mathbf{y} = [y(\omega_{r1}) \cdots y(\omega_{rJ})]^{\mathrm{T}}$ is the Fourier transform of the observed time series synchronized to the pulse transmission for J discrete frequencies. α is the complex scalar factor for unknown amplitude scaling and a frequency independent phase shift. $\mathbf{E}(\xi) = \mathrm{diag}[e^{i\omega_{r1}\xi} \cdots e^{i\omega_{rJ}\xi}]$ where ξ is the timing error between the source and receiver clocks. The corresponding replica field $\mathbf{d}(\mathbf{m}) = [\psi(\omega_{r1}, \mathbf{m}) \cdots \psi(\omega_{rJ}, \mathbf{m})]^{\mathrm{T}}$ is generated using Eq. (15) with vector $\mathbf{m}$. $\mathbf{m}$ is a subset of forward model parameters that are being optimized (see Fig. 1).

The distribution of the error vector $\mathbf{w} = [w(\omega_{r1}) \cdots w(\omega_{rJ})]^{\mathrm{T}}$ defines the likelihood function. Error comprises ambient noise and modeling errors. In high SNRs, array-coherent frequency-incoherent techniques often neglect ambient noise but recognize modeling errors as dominant.[28,29]

For low SNR frequency-coherent processing, the colored ambient noise might be a significant source of error. The frequency-dependent noise is modeled as a wide sense stationary (WSS) noise $u[n]$ with power spectral density $\gamma_u P_{uu}(\omega_r)$ where γ_u is a scaling factor, used for varying SNR in simulations and scaling the noise spectrum in inversions using real data. $P_{uu}(\omega_r)$ is estimated from the noise only data prior to signal transmission.

Taking a N-point discrete Fourier transform (DFT) of $u[n]$, let $\mathbf{w}$ be the DFT of $\mathbf{u}$ evaluated at frequencies $[\omega_{r1} \cdots \omega_{rJ}]$ with $J \leq N$. We will define the frequency domain noise $\mathbf{w}$ as complex Gaussian with mean $\mathrm{E}[\mathbf{w}] = \mathbf{0}$ for $\omega_r \neq 0$ and autocovariance[30]

$$\mathbf{C}_{\mathbf{w}} = \mathrm{E}[\mathbf{w}\mathbf{w}^{\mathrm{H}}] = N\gamma_u \mathrm{diag}[P_{uu}(\omega_{r1}) \cdots P_{uu}(\omega_{rJ})]. \tag{17}$$

Thus, it is assumed that the error vector $\mathbf{w} \sim \mathcal{CN}(\mathbf{0}, \mathbf{C}_{\mathbf{w}})$. Factoring $\mathbf{C}_{\mathbf{w}} = \gamma \tilde{\mathbf{C}}_{\mathbf{w}}$ with reparameterized $\gamma = N\gamma_u$, the likelihood function can be expressed as[31]

$$L(\xi, \mathbf{m}, \alpha, \gamma) = \frac{1}{(\pi\gamma)^J |\tilde{\mathbf{C}}_{\mathbf{w}}|} \times \exp\{-[\mathbf{y} - \alpha\mathbf{b}(\xi, \mathbf{m})]^{\mathrm{H}} \tilde{\mathbf{C}}_{\mathbf{w}}^{-1} \times [\mathbf{y} - \alpha\mathbf{b}(\xi, \mathbf{m})]/\gamma\}. \tag{18}$$

The unknown complex scaling factor α and noise parameter γ are estimated by maximum likelihood estimation (MLE). Computing the MLE of α, $\hat{\alpha}$, and γ, $\hat{\gamma}$ via $[\partial \ln L(\xi, \mathbf{m}, \alpha, \gamma)]/(\partial\alpha) = 0$ and $[\partial \ln L(\xi, \mathbf{m}, \alpha, \gamma)]/(\partial\gamma) = 0$, respectively, gives

$$\hat{\alpha} = \frac{\mathbf{b}^{\mathrm{H}} \tilde{\mathbf{C}}_{\mathbf{w}}^{-1} \mathbf{y}}{\mathbf{b}^{\mathrm{H}} \tilde{\mathbf{C}}_{\mathbf{w}}^{-1} \mathbf{b}}, \tag{19}$$

$$\hat{\gamma} = \frac{(\mathbf{y} - \alpha\mathbf{b})^{\mathrm{H}} \tilde{\mathbf{C}}_{\mathbf{w}}^{-1} (\mathbf{y} - \alpha\mathbf{b})}{J} = \frac{\beta(\xi, \mathbf{m})}{J}, \tag{20}$$

where $\beta(\xi, \mathbf{m})$ is the covariance-weighted Bartlett function,[28] obtained by substituting $\alpha = \hat{\alpha}$, defined as

$$\beta(\xi, \mathbf{m}) = \mathbf{y}^{\mathrm{H}}\tilde{\mathbf{C}}_{\mathbf{w}}^{-1}\mathbf{y} - \frac{|\mathbf{y}^{\mathrm{H}}\tilde{\mathbf{C}}_{\mathbf{w}}^{-1}\mathbf{b}|^2}{\mathbf{b}^{\mathrm{H}}\tilde{\mathbf{C}}_{\mathbf{w}}^{-1}\mathbf{b}}. \tag{21}$$

Substituting Eqs. (19)–(21) into Eq. (18), the optimized inversion parameters obtained via the maximization of the log-likelihood function are

$$\begin{aligned}\{\xi, \mathbf{m}\}_{ML} &= \arg\max_{\xi, \mathbf{m}}[\ln L(\xi, \mathbf{m})] \\ &= \arg\min_{\xi, \mathbf{m}}[J \ln \beta(\xi, \mathbf{m}) \\ &\quad + J(\ln \pi - \ln J + 1) + \ln|\tilde{\mathbf{C}}_{\mathbf{w}}|] \\ &= \arg\min_{\xi, \mathbf{m}}[10 \log_{10}\Phi(\xi, \mathbf{m})],\end{aligned} \tag{22}$$

where the cost function

$$\Phi(\xi, \mathbf{m}) = \frac{\beta(\xi, \mathbf{m})}{\mathbf{y}^{\mathrm{H}}\tilde{\mathbf{C}}_{\mathbf{w}}^{-1}\mathbf{y}} = 1 - \frac{|\mathbf{y}^{\mathrm{H}}\tilde{\mathbf{C}}_{\mathbf{w}}^{-1}\mathbf{b}|^2}{\mathbf{y}^{\mathrm{H}}\tilde{\mathbf{C}}_{\mathbf{w}}^{-1}\mathbf{y}\mathbf{b}^{\mathrm{H}}\tilde{\mathbf{C}}_{\mathbf{w}}^{-1}\mathbf{b}} \tag{23}$$

is the normalized covariance-weighted Bartlett function. In $\mathbf{y}^{\mathrm{H}}\tilde{\mathbf{C}}_{\mathbf{w}}^{-1}\mathbf{b}$, the correlation between the measured and the replica spectrum is inversely weighted by the noise spectrum.

C. Synthetic aperture formation

Extending the temporal duration of the source to a train of P repeated transmissions, the source spectrum is

$$S(f) = \sum_{p=0}^{P-1} \exp(i2\pi f p T_r) S_c(f), \tag{24}$$

where T_r is the pulse repetition interval (PRI) and $S_c(f)$ is the spectrum of the common or repeated source transmission. Substituting Eq. (24) into Eq. (15) also extends the moving source or receiver trajectory field. In essence, a synthetic aperture is formed since the waveguide Doppler field is computed by integrating over the source and receiver horizontal trajectory referenced to the source-receiver separation at $t = 0$. The source-receiver synthetic aperture length or relative displacement is $PT_r(v_s - v_r)$ m.

The extended duration transmission and relative motion means that the synthetic aperture length is longer than the one with a single LFM pulse. As explained later in Sec. III C 1, without the waveguide Doppler model, the mismatch between the measured (waveguide Doppler) and the replica (uniform Doppler[6,26]) complex field will increase with P and synthetic aperture length. This mismatch error then will map into the parameter estimation error.

D. Source spectrum

A common broadband source used in geoacoustic inversion is the LFM pulse. It is the source used for the simulations in Sec. III and experimental data analysis in Sec. IV. Comparing Eq. (16) with other models[25–27] and examining Eq. (15), the source spectrum is coupled within, and noncommutable with, the integral of the Green's function due to source/receiver motion. This coupling results in very fine frequency indexing to the source spectrum for each mode. Hence, an analytic Fourier expression of the source spectrum is desirable. The time domain expression of the LFM pulse is

$$s_c(t) = \sin\left[\frac{\pi(f_2 - f_1)t^2}{T} + 2\pi f_1 t\right], \tag{25}$$

where f_1 and f_2 is the start and stop frequency, respectively, and T is the pulse width. Using the same Fourier transform convention,[18,19] the frequency domain expression of the LFM pulse is

$$\begin{aligned}S_c(f) &= \int_0^T \sin\left[\frac{\pi(f_2 - f_1)t^2}{T} + 2\pi f_1 t\right] e^{i2\pi f t} dt \\ &= \frac{B}{4\sqrt{\pi}}\, e^{-B^2(f_1+f)^2}\Big(e^{2B^2(f_1^2+f^2)} \\ &\quad \times \{\mathrm{erf}[B(f_2 - f)] - \mathrm{erf}[B(f_1 - f)]\} \\ &\quad + i\mathrm{erf}[iB(f_2 + f)] - i\mathrm{erf}[iB(f_1 + f)]\Big),\end{aligned} \tag{26}$$

where $\mathrm{erf}(z) = (2/\pi)\int_0^z e^{-t^2} dt$ is the error function and $B = (\sqrt[4]{-1}\sqrt{\pi T})/\sqrt{f_2 - f_1}$.

Figure 2 shows a section of the source spectrum for various P LFM pulses using Eqs. (24) and (26). Magnitudes have been normalized by the single LFM spectrum magnitude for comparison. The overall source spectrum $S(f)$ will result in periodic spectral peaks occurring every $1/T_r$ for $P \geq 2$. The null-to-null bandwidth for each peak is $2/(PT_r)$. In addition, the spectral peaks increase 6 dB for every doubling of P. Correspondingly, the noise spectrum level only increases by 3 dB, Eq. (17). These spectral peaks are good frequency sampling points although, as shown later in Sec. III C 2, source/receiver motion will require more frequency sampling points around these peaks. The overall source spectrum of multiple LFM pulses also approaches a multi-tone comb resulting in an inversion technique that is sensitive to waveguide Doppler, see Sec. III C 1.

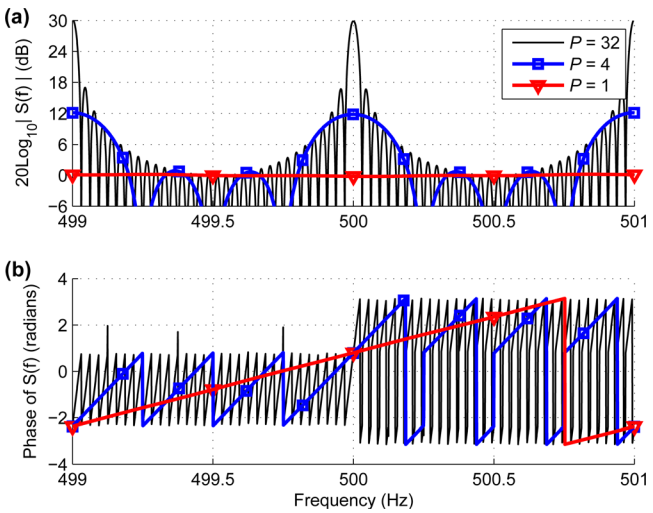

FIG. 2. (Color online) A section of the 100–900 Hz ($T_r = T = 1$ s) source spectrum for $P = [1, 4, 32]$ LFM pulses in (a) magnitude and (b) phase.

TABLE II. Baseline model parameters.

Model parameters	Value
Src range, r_0 (m)	2000
Src depth, z_s (m)	30
Rcv depth, z (m)	45
Src vel., v_s (m/s)	2.5
Rcv vel., v_r (m/s)	0
Water depth, z_w (m)	80
Sed. depth, h_{sed} (m)	22
Sed. density, ρ_{sed} (g/cm^3)	1.8
Sed. attn., α_{sed} (dB/λ)	0.2
Sed. top. vel., c_1 (m/s)	1630
Sed. vel. slope, s (1/s)	0
Bot. density, ρ_{bot} (g/cm^3)	2.1
Bot. attn., α_{bot} (dB/λ)	0.2
Bot. vel., c_b (m/s)	1740

III. SIMULATIONS

Based on the theory, this section will demonstrate three main points. First, Sec. III A provides the inversion sensitivities for a simple static source/receiver setup using a single LFM pulse transmission. Then, in Sec. III B, Monte Carlo inversions at a fixed SNR for a static source/receiver show that estimation uncertainty is reduced by coherently exploiting multiple LFM pulse transmissions. Finally, in Sec. III C, for a moving source and static receiver case, both waveguide Doppler and a denser frequency sampling scheme are needed to preserve the uncertainty reduction.

The ocean model is illustrated in Fig. 1. The model parameters are tabulated in Table II. These range-independent parameters were based on previous SW06 inversion results.[32–35] The source is a 100–900 Hz LFM pulse with 1 s pulse width and PRI. Colored noise was generated using the measured power spectrum of SW06 noise data (see Fig. 9). The source is moving towards the static receiver. Frequency sampling usually is fixed at $\Delta f = 5$ Hz. The forward model used is KRAKEN.[36]

A. Sensitivity analysis for static source and receiver with a single LFM pulse

Sensitivity plots for several parameters of a single LFM pulse noiseless reception and a static source and a receiver is simulated in Fig. 3. For each parameter, sensitivity plot is created by sweeping the parameter under test in the cost function while keeping the rest of the parameters at their baseline value. Because the cost function Φ approaches negative infinity in dB for a perfectly matched field, the maximizing function $10\log_{10}(1-\Phi)$ is plotted instead. As expected, the geometric parameters such as water depth and source range are the most sensitive. These are followed by sediment velocity and density with intermediate sensitivity. The remaining bottom related parameters, such as sediment thickness and bottom halfspace velocity, are the least sensitive.

B. Multiple LFM pulses for a static source and receiver

Low SNR scenarios may arise from propagation loss or source level restrictions. In this simulation, with SNR fixed

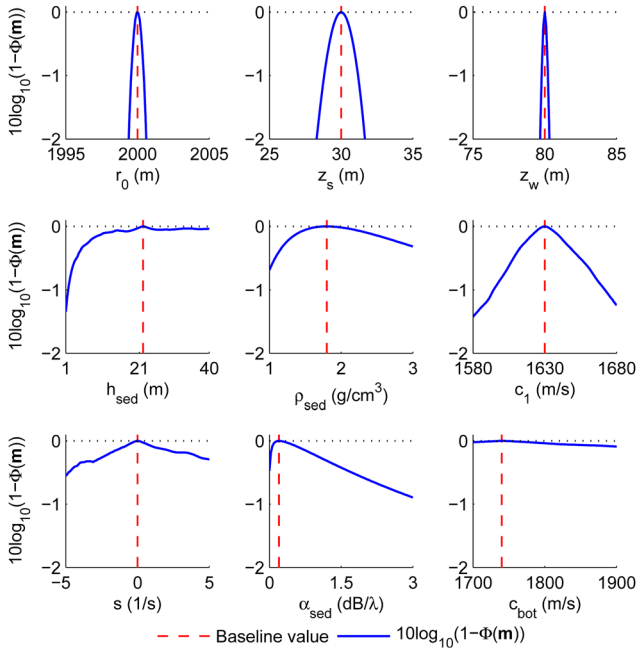

FIG. 3. (Color online) Sensitivity plots for a static source/receiver case.

at −6 dB (calculated over LFM pulse bandwidth), coherently processing multiple LFM pulse receptions [source spectrum is Eq. (24)] can reduce data uncertainty (see Fig. 4). Frequency sampling is fixed at $\Delta f = 5$ Hz. Monte Carlo inversions of 200 noise realizations per P setting were carried out to assess uncertainty of the parameter estimates. Only four representative parameters (z_s, h_{sed}, c_1, and c_{bot}) of various sensitivities were chosen to keep the parameter search space small. The inversions were optimized using a genetic algorithm (GA). The values of the GA parameters are as follows: population size, 16; selection, 0.5; crossover, 0.8; mutation, 0.1; iterations, 8; and parallel populations, 8. Their parameter estimate distributions are plotted in Fig. 4 as histograms. The histograms are more informative than error bars (mean and standard deviation) as the cost surface

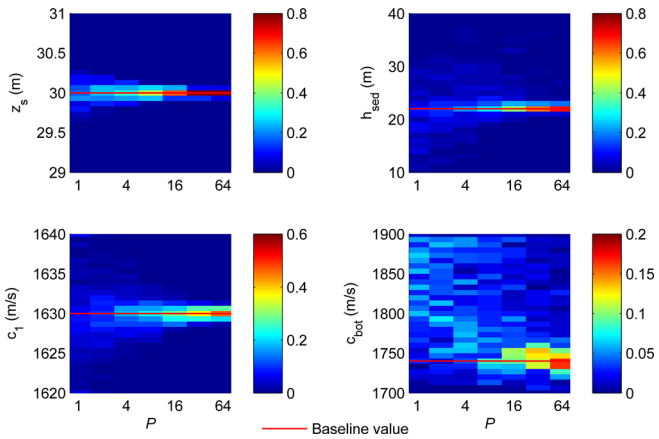

FIG. 4. (Color online) Histograms of four-parameter inversions for the static source and receiver case. The intensity plots are the histograms for the Monte Carlo simulation corresponding to 200 noise realizations with SNR fixed at −6 dB and number of LFM pulses $P = [1, 2, 4, 8, 16, 32, 64]$. Histograms are stacked vertically along the horizontal axis. Color bars indicate the relative frequency values.

may be skewed or have multiple minima giving rise to skewed or multiple peak histograms. Generally, bottom parameters (sediment thickness h_{sed} and bottom velocity c_b) required higher P values for low estimation uncertainty.

C. Multiple LFM pulses for a moving source and static receiver

For a moving source and static receiver case, there are mode-dependent frequency and wave number shifts. It is shown here that waveguide Doppler theory and a denser frequency sampling scheme are needed to exploit multiple LFM pulses coherently.

1. Applicability of waveguide Doppler processing

Waveguide Doppler[16–21] is more significant in certain circumstances. It depends on the type of shallow water waveguide, the source spectrum and the length of the source/receiver trajectory. When the bottom is hard, higher order modes will be relatively stronger than those for soft bottom. Correspondingly, the waveguide Doppler phenomenon will be more pronounced. Another factor is the source spectrum. Because a waveguide Doppler field traces back to several source frequencies, see Eq. (15), source spectrums (complex value) that vary more with frequency are more sensitive to waveguide Doppler. Last, the replica field for a moving source/receiver trajectory often is approximated with a static point field computation. Because of the long observation time, this fails when the synthetic aperture exceeds several wavelengths during signal transmission and reception, respectively.[20] Here, the disparity arises from a moving source with a source spectrum consisting of concatenated LFM pulses. In this case, waveguide Doppler modeling is needed.

In Fig. 5(a), the moving source simulation is similar to previous static simulation except that the measured field is based on waveguide Doppler theory while the replica field assumes uniform Doppler.[6,26] Under the uniform Doppler assumption, the source spectrum is frequency shifted as if in free space [Eq. (27)]. The resulting source spectrum $S[\omega_s^{(v_s)}]$ then is propagated through the normal mode model, where all the modes are given the same Doppler shift for a given frequency,

$$\omega_s^{(v_s)} = \omega_r \left[1 - \frac{v_s}{c(z_s)}\right]. \tag{27}$$

At a given receiver frequency, the waveguide Doppler field comprises several contributing source frequencies due to mode-dependent Doppler [Eq. (15)]. When uniform Doppler is assumed, the source spectrum gets decoupled from the Green's function since Doppler is mode independent. Therefore, a uniform Doppler field has only one contributing source frequency defined in Eq. (27). The mismatch between the waveguide and the uniform Doppler field increases with increasing P. This is because increasing P also increases the phase response slope of the source spectrum [see Fig. 2(b)]. These translate to parameter estimation errors. This is observed in Fig. 5(a) (source depth z_s and top

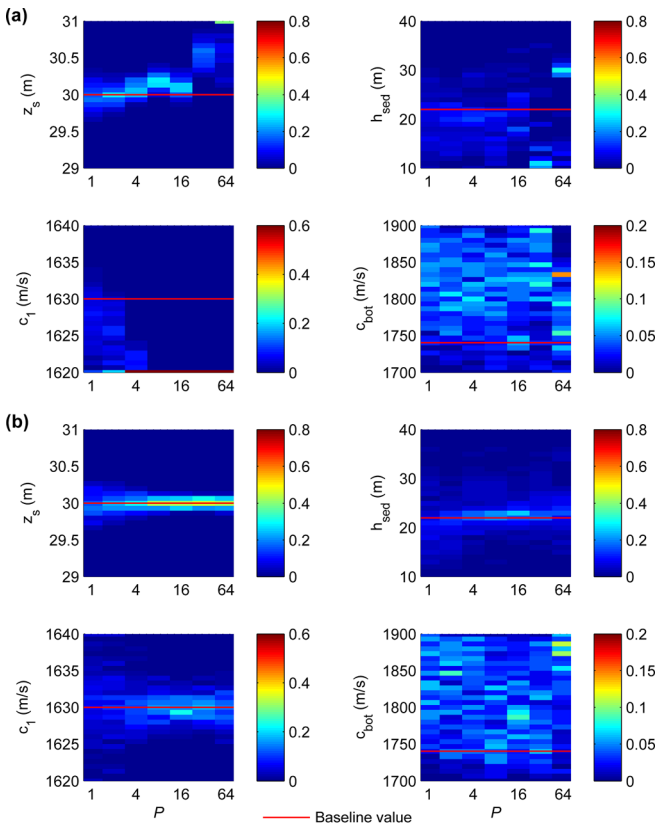

FIG. 5. (Color online) Histograms of four-parameter inversions for the moving source/static receiver case, SNR $= -6$ dB, and number of LFM pulses P with corresponding synthetic aperture of [2.5, 5, 10, 20, 40, 80, 160] m for (a) uniform Doppler, and (b) waveguide Doppler.

sediment velocity c_1). Generally, the parameter estimation histograms degrade with increasing P.

If no source motion is incorporated in the replica field, the estimation histograms will degrade even more (not shown here). When the replica is generated using waveguide Doppler theory, Fig. 5(b), there is decreasing parameter uncertainty for increasing $P \leq 16$. Thereafter, the parameter estimation degrades due to inadequate frequency sampling. In both cases, frequency sampling is done every 5 Hz for $P \leq 4$ since the peaks are either not present or difficult to detect due to noise (see Fig. 2). However, for $P \geq 8$, frequency sampling is done at every five spectral peaks (peaks are slightly more than $1/T_r = 1$ Hz apart due to Doppler).

2. Frequency sampling

Ideally, all FFT frequencies in the LFM pulse band should be included in the processing. Practically, frequency sampling can be done at a far wider interval as long as there is no range aliasing lobes in the cost surface within the range search space.[37] The frequency sampling interval also should sample adequately the frequency-selective faded or interference-fringe received spectrum which contains information on the shallow water multipath impulse response.[38,39] This sampling criterion is approximately the inverse of the maximum multipath delay spread.[11]

A moving source adds complexity to the frequency sampling approach. Figure 6(a) is a simulated noiseless received

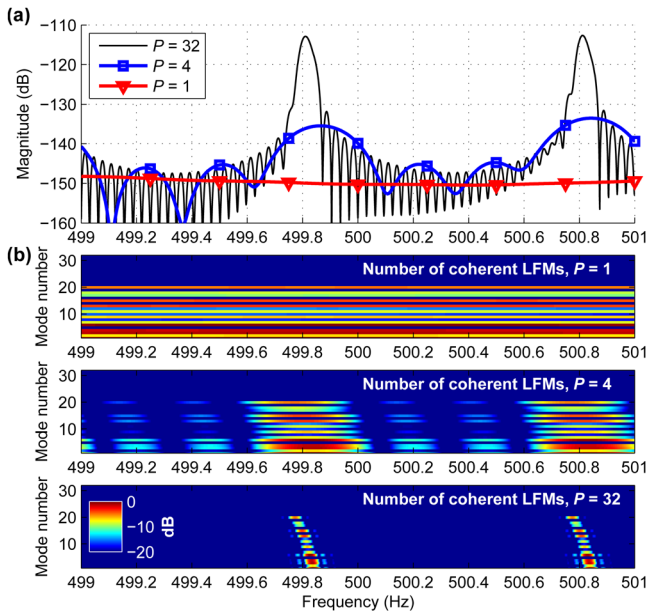

FIG. 6. (Color online) (a) Simulated received spectrum (499–501 Hz) for $P = [1, 4, 32]$ with corresponding synthetic aperture of [2.5, 10, 80] m. (b) Same as (a) but prior to modal summation.

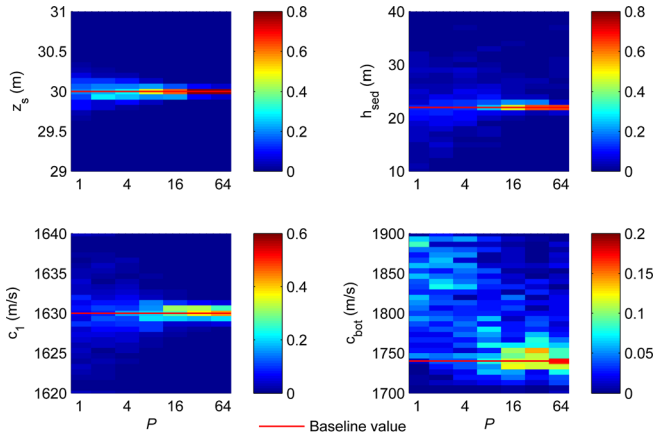

FIG. 7. (Color online) Histograms of four-parameter waveguide Doppler based inversions for the moving source/static receiver case, SNR $= -6$ dB and number of LFM pulses P with corresponding synthetic aperture of [2.5, 5, 10, 20, 40, 80, 160] m. Frequency sampling within ± 0.2 Hz band at every five spectral peaks.

spectrum from a moving source with spectrum shown in Fig. 2 propagating through the waveguide Doppler model described in Fig. 1 and Table II. The 6 dB peak increments observed in the source spectrum for each doubling of pulses (see Fig. 2) is less consistent in the received spectrum in Fig. 6(a). For example, the 30 dB difference between $P = 1$ and $P = 32$ peaks in Fig. 2 corresponds to 36 dB in Fig. 6(a). Prior to modal summation, the spectrum for each mode is plotted in Fig. 6(b) to show their different modal Doppler shifts. Contrary to the static case, the mode-dependent Doppler in the complex-valued $S[\omega_s^{(k_n)}]$, as indicated in Fig. 6(b) and Eq. (15), will impose a different inter-modal interference which may cause the peak increments to deviate from 6 dB per doubling of pulses.

Note that as P increases, the spectral main lobes becomes smaller. Concentrating the energy into a narrowband lobe such that it is not larger than the Doppler spread, which is defined here as the Doppler difference between the most and least significant modes, will cause the modes to influence separate frequency bands. For $P = 32$, the peaks in Fig. 6(a) will have less influence of higher order modes due to the different modal Doppler shifts and stronger lower order modes [Fig. 6(b)]. Hence, sampling the spectral peaks will result in the loss of information from higher order modes. This has two effects.[40] First, there will be a loss of deeper bottom penetration as higher order modes have higher vertical wave numbers (higher grazing angles). Second, there will be a loss of bottom resolution due to the loss of shorter vertical wavelength of higher order modes. These give higher estimation uncertainty for the bottom parameters as P becomes large, which is evident in Fig. 5(b) (see histograms for c_1 and h_{sed} for $P > 16$).

To correct this, it is necessary to sample multiple frequency points per spectral lobe in order to include all the modes within the Doppler spread, which in this case is ± 0.2 Hz. The results in Fig. 7 are obtained with this sampling approach and the performance is as good as the static case in Fig. 4. To save on computation, the replica field is evaluated only at the peak frequencies. The fields for the surrounding frequencies are computed using the modal functions at the peak frequencies and extrapolated wave numbers via Taylor's approximation $k_n(\omega_r + \delta\omega_r) \approx k_n(\omega_r) + \delta\omega_r / u_{rn}$ [see Eq. (13)].

IV. EXPERIMENTAL DATA ANALYSIS

The SW06 experiment was carried out near the shelf break on the New Jersey continental shelf from July to September 2006. A low SNR data set was chosen with a constant radial velocity moving source and static receiver over a range independent track, see Fig. 8. The acoustic data is from a 44.6 m deep single receiver, Channel 8 of a vertical line array (VLA1). On JD238 2029 UTC ($t = 0$), 64 LFM pulse (100–900 Hz) transmissions were made from a 30 m deep J-15 source towed by the R/V Knorr at 2.5 m/s between Waypoint 5 (WP5) and Waypoint 6 (WP6) towards VLA1.

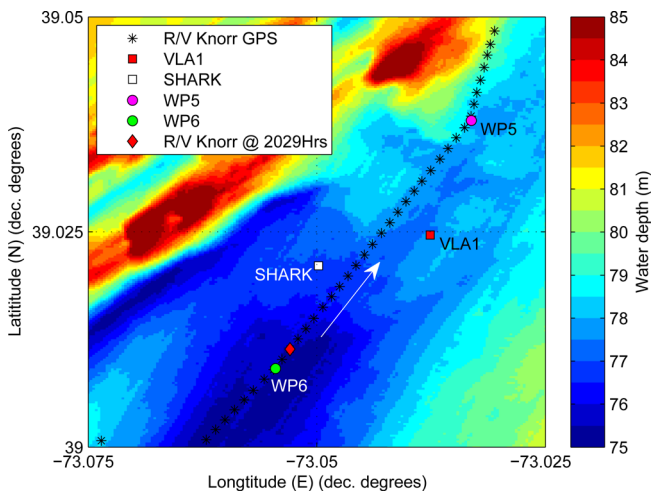

FIG. 8. (Color online) SW06 experiment site, bathymetry, source, and receiver positions on JD238 (26 August 2006) 2000–2059 UTC.

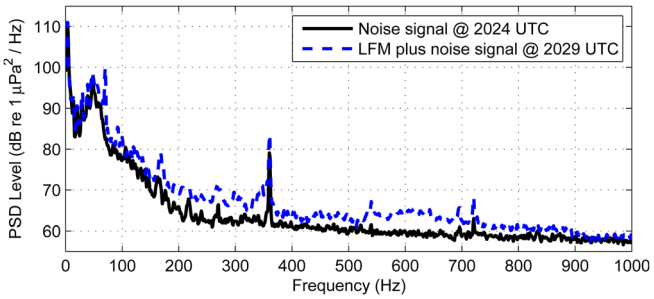

FIG. 9. (Color online) Power spectral density of received signal.

The LFM pulse width is 1 s and is repeated every second. Correspondingly, the towed source displacement or synthetic aperture is 2.5 m/s × 64 s = 160 m long. The R/V Knorr GPS range to VLA1 was 1981 m. Based on the ship and VLA1 positions, the actual source to VLA1 distance at $t = 0$ is estimated to be 2050–2100 m.

The power spectral density (PSD) of the received signal in Fig. 9 was generated from 60 s data. The SNR of the received signal was estimated to be 0.4 dB. Noise only data at 2024 UTC was added to the signal plus noise data at 2029 UTC to lower the SNR to −6 dB.

The nearest conductivity-temperature-depth (CTD) measurement was at 1905 UTC and about 1 km southwest of Waypoint 6 (WP6). Because of the lack of CTD measurements during this period and location, sound speed profile inversion using empirical orthogonal functions[32,33,41] (EOFs) were based on sound speed profiles (SSPs) derived from thermistors along the SHARK array, which have less depth resolution than the CTD measurements. On the other hand, the SHARK array is located in the middle between the source and VLA1. It also measured the temperatures every 30 s. To estimate the SSP, a constant salinity was assumed. Figure 10(a) shows the SHARK derived SSPs over 4 h. The SSPs varied between 10 and 70 m with the greatest velocity change at 40 m. The water depth at the SHARK array was 79 m. In Fig. 10(b), the mean SSP and EOFs are derived from the SHARK SSPs.

Bottom reflection measurements and other analyses were done at the VLA1 site.[32–35] The bottom is characterized with a clay-rich sediment layer of lower velocities that is estimated to be around 1630 m/s ± 20 m/s. The R reflector was noted at 22 m ± 3 m based on vertical incidence chirp data.

A. Matched-field geoacoustic inversion

The inversion search bounds were set for the forward model depicted in Fig. 1 based on the background information at the experiment site. These are tabulated in Table III. In addition, sensitivity analysis shows that parameters could be grouped into sensitive and insensitive sets. Sensitive parameters will usually dominate the inversion algorithm giving poor estimation results for insensitive parameters. Sensitive parameters are source range, source, receiver and water depth, source velocity, timing error, and EOF1 and EOF2 coefficients. The matched field inversion algorithm used here is based on a multi-step approach[35] where the first

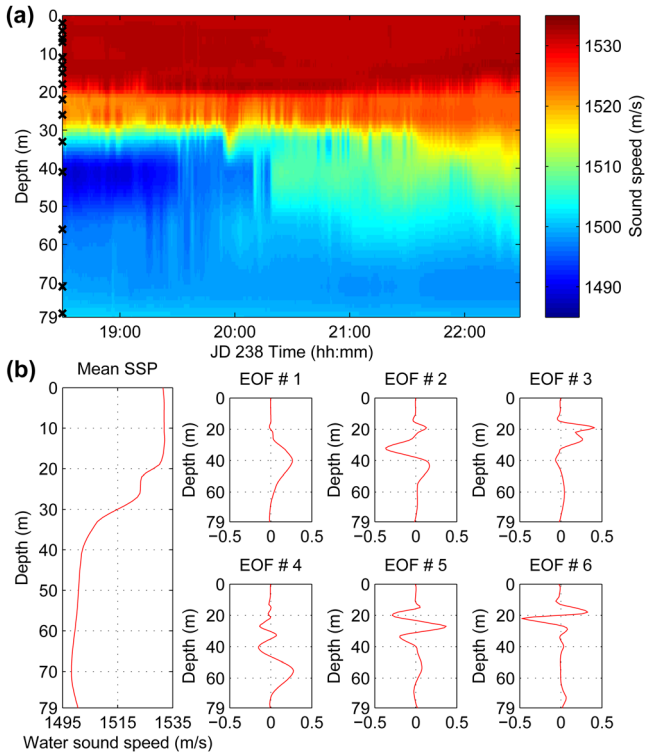

FIG. 10. (Color online) (a) SW06 SHARK interpolated sound speed profile from 1830–2229 UTC. Temperature sensor depths (×): 2, 4, 6, 7, 11, 13, 15, 18, 22, 26, 33, 41, 56, 71, and 78 m. (b) Mean SSP and EOFs derived from SHARK SSPs.

step inversion inverted both sensitive and insensitive parameters and the second step inversion refined the results by significantly reducing (by a factor of 5) the search bounds of the sensitive parameters with the first step results. This gave better convergence rates for the insensitive parameters. GA performed the minimization of the cost function Eq. (22).

TABLE III. SW06 data inversion parameters search bounds and results for $P = 64$.

Model parameters	Lower bound	Upper bound	Waveguide Doppler	Uniform Doppler
Src range, r_0 (m)	2050	2100	2075	2064
Src depth, z_s (m)	27	33	30.1	30.9
Rcv depth, z (m)	41	47	42.6	44.8
Timing error, ξ (msec)	−5	5	−1.3	2
Src vel., v_s (m/s)	2.3	2.8	2.55	2.53
Water depth, z_w (m)	72	82	75.6	77.4
EOF1 coef.	−50	50	30.1	5.9
EOF2 coef.	−25	25	3.8	3.6
EOF3 coef.	−10	10	1.2	0.6
EOF4 coef.	−10	10	−2.0	−1.9
EOF5 coef.	−10	10	6.1	7.5
EOF6 coef.	−6	2.5	−1.7	−3.0
Sed. dens., ρ_{sed} (g/cm^3)	1	2.5	2.01	1.73
Sed. attn., α_{sed} (dB/λ)	0.001	3	1.1	2.3
Sed. top. vel., c_1 (m/s)	1500	1700	1644	1549
Sed. vel. slope, s (1/s)	−10	10	6.2	3.5
Sed. thickness, h_{sed} (m)	10	40	22.8	22.2
Bot. vel., c_b (m/s)	1700	1900	1795	1812

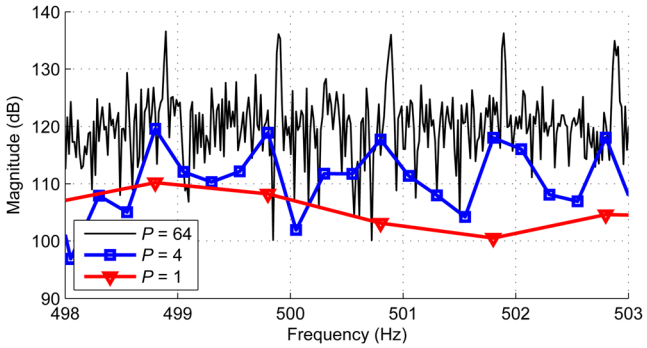

FIG. 11. (Color online) Section of SW06 received signal spectrum with LFM pulses $P = [1, 4, 64]$.

The values of the GA parameters are as follows: population size, 512; selection, 0.5; crossover, 0.8; mutation, 0.02; iterations, 32; and parallel populations, 12. The search bounds for the first six parameters in Table III were set related to direct measurements, for example, GPS readings and the source depth sensor. The search bounds for the water SSP EOFs coefficients were determined from the distributions of the EOFs coefficients. The bounds for the last six bottom parameters in Table III were set based on empirical data[42] and some SW06 related publications.[32–35]

Pre-processing of the single receiver data include LFM pulse matched filtering for coarse synchronization, data segmentation into various numbers of LFM pulse concatenations and finally, the fast Fourier Transform (FFT) of each data segment is carried out to obtain the measured field in the frequency domain. Figure 11 shows the spectrum for $P = [1, 4, 64]$ where the spectral peaks for the 4 and 64 LFM pulses spectra can be seen clearly. The peaks in Fig. 11 are in agreement with the noise-free simulation in Fig. 6(a). Because of a limited number of available LFM pulses and the large 18-parameter search space, estimation histograms, such as those simulated, cannot be replicated from the SW06 data. Only the $P = 64$ inversion results are shown here where the synthetic aperture length is 160 m long. The receiver frequencies were indexed according to the spectral peaks. Because $1/T_r = 1$ Hz, there are potentially 800 spectral peaks. For computational reasons, the frequency sampling is approximately every 5 Hz from 100–700 Hz. For each peak, frequency samples within ± 0.2 Hz were included. The FFT resolution is $(T_r P)^{-1}$.

Table III tabulates the inversion results using the waveguide Doppler model and the uniform Doppler model for 64 LFM pulses. For the waveguide Doppler model results, the estimated sediment thickness, velocity, and density are consistent with other published results[32–35] at the MPL-VLA1 site. For example, these inversion results range from 1600–1650 m/s for the top sediment velocity and 21–25 m for the sediment thickness.[32–35] However, the sediment profile is estimated to have a positive gradient of about 6.2 m/s per m, while others[33–35] have estimated or assumed straight and negative gradient profiles. The top sediment velocity profile of the uniform Doppler model was not consistent and had a -100 m/s deviation when compared with other published results.[32–35] This also agree with the uniform Doppler simulation results

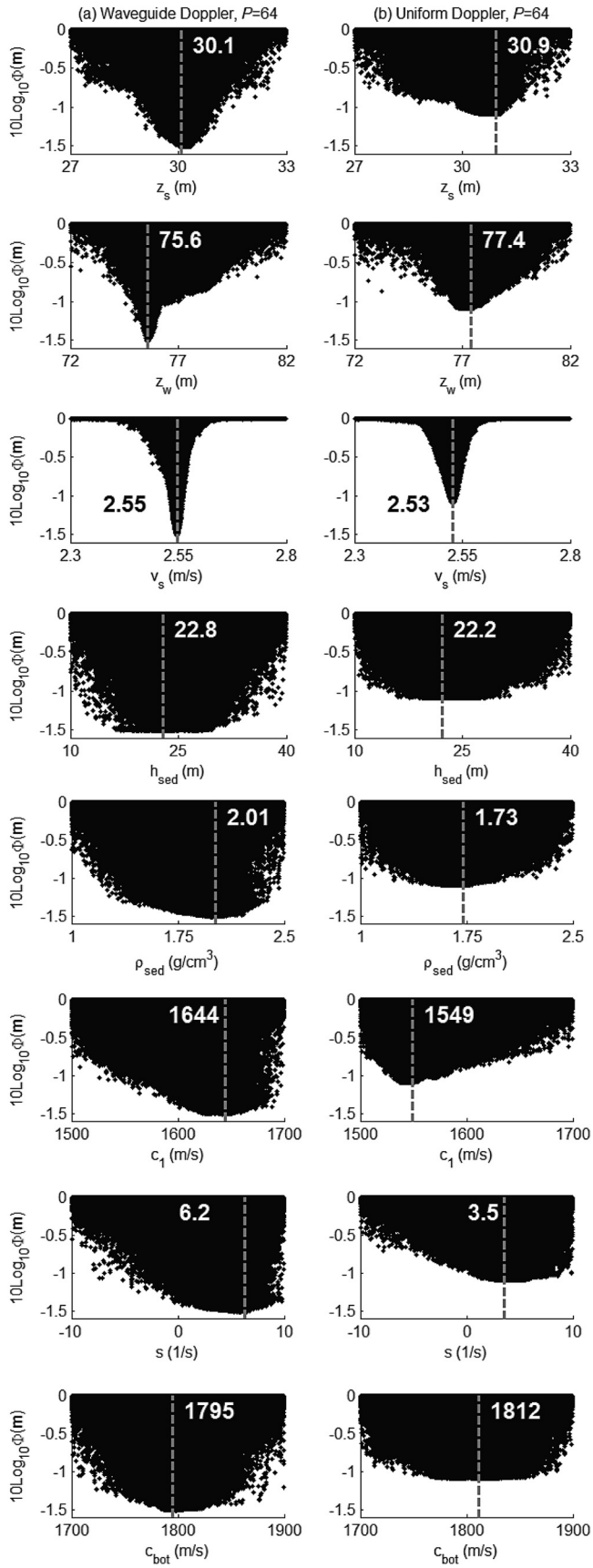

FIG. 12. SW06 64 s data inversion scatterplots for $P = 64$ with a synthetic aperture of 160 m for (a) waveguide Doppler model and (b) uniform Doppler model. The vertical dashed line shows the final inversion results with SNR ≈ -6 dB.

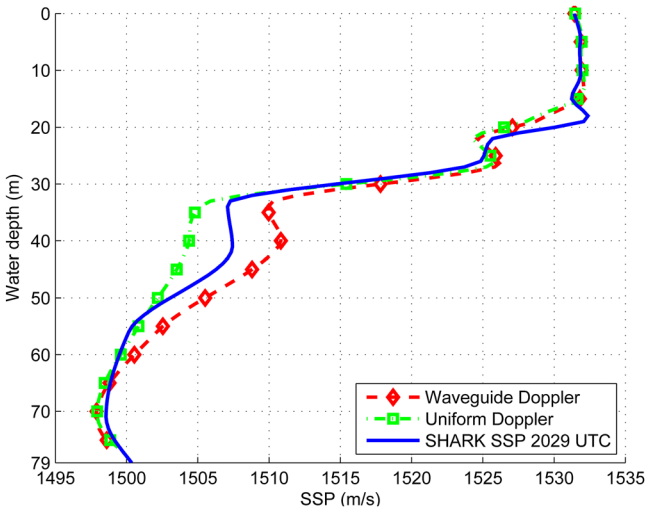

FIG. 13. (Color online) SSP inversion results using SW06 experimental data and $P = 64$ with waveguide Doppler and uniform Doppler models.

where the sediment velocity profile is negatively biased for increasing P, see Fig. 5(a) for c_1 top sediment velocity.

Scatterplots can be used to compare sensitivities and estimation uncertainties between the two inversions. Figure 12 shows the scatterplots, for selected parameters, of the cost function values plotted for waveguide Doppler and uniform Doppler evaluated in GA ($P = 64$). The scatterplots give information about the real sensitivities of the parameters by observing the envelopes of the scatterplots. A sharper minimum usually indicates lower estimation uncertainty. The geometric parameters, such as source depth, show high sensitivities since time/phase delay is important in signal correlation. The inversion is also sensitive to source radial velocity and could only tolerate mismatches on the order of 0.1 m/s [third row of Fig. 12(a)]. Source velocity sensitivity increases with P and synthetic aperture. Overall, the waveguide Doppler scatterplots indicate higher sensitivities and hence lower estimation uncertainties than the uniform Doppler. The waveguide Doppler scatterplots also show a lower minimum cost value indicating that it is a better model than the uniform Doppler. These observations are consistent with the simulation results.

Figure 13 shows the estimated water column SSPs using the waveguide Doppler and the uniform Doppler models. Because the SSPs are range dependent in SW06,[32] the SHARK SSP measured at 2029 UTC is not a good substitute for a range independent SSP and, it gave inconsistent estimation results and a higher cost value. The EOFs have allowed the inversion to optimize the best range-independent SSP which is also the one using the waveguide Doppler model.

V. CONCLUSIONS

This paper presented a single-receiver, broadband, frequency-coherent matched-field inversion approach that exploits coherently repeated transmissions at low SNR for a moving source and receiver. The long observation time creates a synthetic aperture due to relative source-receiver motion. The source transmission consisted of multiple LFM pulses with a spectrum that approaches a multi-tonal comb with increasing Doppler sensitivity as the number of pulses increase. As a result, this requires incorporating waveguide Doppler in normal mode theory and increased frequency sampling around the spectral peaks.

The waveguide Doppler inversion approach was demonstrated with low SNR data from the Shallow Water 2006 experiment with a moving source and static receiver configuration and 100–900 Hz LFM pulse transmissions. The inversion results agreed well with published results from the same site. On the other hand, the uniform Doppler model resulted in a sediment profile with a -100 m/s deviation, higher cost function value, and less sensitive scatterplots.

ACKNOWLEDGMENTS

This work was supported by the Office of Naval Research Grant No. N00014-11-0320. In addition, B.A.T. is supported by DSO National Laboratories of Singapore. The authors thank William Kuperman and Hee Chun Song for insightful discussions on Doppler in a shallow water waveguide, and Dave Ensberg for his help with the SW06 data.

[1]J. Bonnel, C. Gervaise, B. Nicolas, and J. I. Mars, "Single-receiver geoacoustic inversion using modal reversal," J. Acoust. Soc. Am. **131**, 119–128 (2012).
[2]J. Bonnel and N. R. Chapman, "Geoacoustic inversion in a dispersive waveguide using warping operators," J. Acoust. Soc. Am. **130**, EL101–EL107 (2011).
[3]J. Bonnel, B. Nicolas, J. I. Mars, and S. C. Walker, "Estimation of modal group velocities with a single receiver for geoacoustic inversion in shallow water," J. Acoust. Soc. Am. **128**, 719–727 (2010).
[4]C. Gervaise, B. G. Kinda, J. Bonnel, Y. Stephan, and S. Vallez, "Passive geoacoustic inversion with a single hydrophone using broadband ship noise," J. Acoust. Soc. Am. **131**, 1999–2010 (2012).
[5]N. F. Josso, C. Ioana, J. I. Mars, and C. Gervaise, "Source motion detection, estimation, and compensation for underwater acoustics inversion by wideband ambiguity lag-Doppler filtering," J. Acoust. Soc. Am. **128**, 3416–3425 (2010).
[6]N. F. Josso, C. Ioana, J. I. Mars, C. Gervaise, and Y. Stephan, "On the consideration of motion effects in the computation of impulse response for underwater acoustics inversion," J. Acoust. Soc. Am. **126**, 1739–1751 (2009).
[7]J. C. Le Gac, M. Asch, Y. Stephan, and X. Demoulin, "Geoacoustic inversion of broad-band acoustic data in shallow water on a single hydrophone," IEEE J. Ocean. Eng. **28**, 479–493 (2003).
[8]S. M. Jesus, M. B. Porter, Y. Stephan, X. Demoulin, O. C. Rodriguez, and E. M. M. F. Coelho, "Single hydrophone source localization," IEEE J. Ocean. Eng. **25**, 337–346 (2000).
[9]P. Hursky, M. B. Porter, M. Siderius, and V. K. McDonald, "High-frequency (8–16 kHz) model-based source localization," J. Acoust. Soc. Am. **115**, 3021–3032 (2004).
[10]J. P. Hermand, "Broad-band geoacoustic inversion in shallow water from waveguide impulse response measurements on a single hydrophone: Theory and experimental results," IEEE J. Ocean. Eng. **24**, 41–66 (1999).
[11]O. Carriere and J.-P. Hermand, "Sequential Bayesian geoacoustic inversion for mobile and compact source-receiver configuration," J. Acoust. Soc. Am. **131**, 2668–2681 (2012).
[12]M. Siderius, P. Gerstoft, and P. L. Nielsen, "Broadband geo-acoustic inversion from sparse data using genetic algorithms," J. Comp. Acoust. **6**, 117–134 (1998).
[13]G. V. Frisk, J. F. Lynch, and S. D. Rajan, "Determination of compressional wave speed profiles using modal inverse techniques in a range-dependent environment in Nantucket sound," J. Acoust. Soc. Am. **86**, 1928–1939 (1989).
[14]S. D. Rajan, G. V. Frisk, K. M. Becker, J. Lynch, G. R. Potty, and J. H. Miller, "Modal inverse techniques for inferring geoacoustic properties in shallow water," in *Important Elements in: Geoacoustic Inversion, Signal Processing, and Reverberation in Underwater Acoustics 2008*, edited by A. Tolstoy (Research Signpost, India, 2008), Chap. 7, pp. 165–234.

[15]D. P. Massa and J. I. Arvelo, "A wideband moving coil electrodynamic transducer system for autonomous underwater vehicle-based geoacoustic inversion," J. Acoust. Soc. Am. **132**, 1920 (2012).
[16]K. E. Hawker, "A normal mode theory of acoustic Doppler effects in the oceanic waveguide," J. Acoust. Soc. Am. **65**, 675–681 (1979).
[17]H. C. Song and A. B. Baggeroer, "The resolution of modal Doppler shifts in a dispersive oceanic waveguide," J. Acoust. Soc. Am. **88**, 268–282 (1990).
[18]H. Schmidt and W. A. Kuperman, "Spectral and modal representations of the Doppler-shifted field in ocean waveguides," J. Acoust. Soc. Am. **96**, 386–395 (1994).
[19]F. B. Jensen, W. A. Kuperman, M. B. Porter, and H. Schmidt, *Computational Ocean Acoustic, Modern Acoustics and Signal Processing*, 2nd ed. (Springer, New York, 2011), pp. 623–629.
[20]P. B. Weichman, "Doppler effects in heterogeneous media with applications to ocean acoustic modeling," Phys. Rev. E **72**, 066602 (2005).
[21]M. H. Brill, "Nonreciprocity of acoustic Doppler effect: Proof and physical mechanism," Phys. Essays **24**, 570 (2011).
[22]S. D. Rajan, J. A. Doutt, and W. M. Carey, "Inversion for the compressional wave speed profile of the bottom from synthetic aperture experiments conducted in the Hudson canyon area," IEEE J. Ocean. Eng. **23**, 174–187 (1998).
[23]K. Ohta, K. Okabe, I. Morishita, G. V. Frisk, and A. Turgut, "Modal inversion analysis for geoacoustic properties of the New Jersey continental shelf in the swat experiments," IEEE J. Ocean. Eng. **34**, 526–538 (2009).
[24]A. Pierce, *Acoustics: An Introduction to Its Physical Principles and Applications* (Acoustical Society of America, New York, 1989), p. 454.
[25]C. Soares and S. M. Jesus, "Broadband matched-field processing: Coherent and incoherent approaches," J. Acoust. Soc. Am. **113**, 2587–2598 (2003).
[26]Y. H. Goh, P. Gerstoft, W. S. Hodgkiss, and C.-F. Huang, "Statistical estimation of transmission loss from geoacoustic inversion using a towed array," J. Acoust. Soc. Am. **122**, 2571–2579 (2007).
[27]C. Soares, S. M. Jesus, and E. Coelho, "Environmental inversion using high-resolution matched-field processing," J. Acoust. Soc. Am. **122**, 3391–3404 (2007).
[28]S. E. Dosso, P. L. Nielsen, and M. J. Wilmut, "Data error covariance in matched-field geoacoustic inversion," J. Acoust. Soc. Am. **119**, 208–219 (2006).
[29]C.-F. Huang, P. Gerstoft, and W. S. Hodgkiss, "On the effect of error correlation on matched-field geoacoustic inversion," J. Acoust. Soc. Am. **121**, EL64–EL69 (2007).
[30]A. Papoulis and S. Pillai, *Probability, Random Variables, and Stochastic Processes*, 4th ed. (McGraw-Hill, New York, 2002), pp. 515, 519.
[31]C.-F. Huang, P. Gerstoft, and W. S. Hodgkiss, "Uncertainty analysis in matched-field geoacoustic inversions," J. Acoust. Soc. Am. **119**, 197–207 (2006).
[32]C.-F. Huang, P. Gerstoft, and W. S. Hodgkiss, "Effect of ocean sound speed uncertainty on matched-field geoacoustic inversion," J. Acoust. Soc. Am. **123**, EL162–EL168 (2008).
[33]Y.-M. Jiang and N. R. Chapman, "Bayesian geoacoustic inversion in a dynamic shallow water environment," J. Acoust. Soc. Am. **123**, EL155–EL161 (2008).
[34]J. W. Choi, P. H. Dahl, and J. A. Goff, "Observations of the R reflector and sediment interface reflection at the shallow water'06 central site," J. Acoust. Soc. Am. **124**, EL128–EL134 (2008).
[35]C. Park, W. Seong, P. Gerstoft, and W. S. Hodgkiss, "Geoacoustic inversion using backpropagation," IEEE J Ocean. Eng. **35**, 722–731 (2010).
[36]M. B. Porter, "The KRAKEN normal mode program," SACLANTCEN Memo. SM-245 (SACLANT Undersea Research Centre, La Spezia, Italy, 1991), Chap. 2.
[37]C. Yardim, P. Gerstoft, and W. S. Hodgkiss, "Range aliasing in frequency coherent geoacoustic inversion," J. Acoust. Soc. Am. **130**, EL154–EL160 (2011).
[38]C. H. Harrison, "The relation between the waveguide invariant, multipath impulse response, and ray cycles," J. Acoust. Soc. Am. **129**, 2863–2877 (2011).
[39]J. P. Hermand and W. I. Roderick, "Acoustic model-based matched filter processing for fading time-dispersive ocean channels: Theory and experiment," IEEE J. Ocean. Eng. **18**, 447–465 (1993).
[40]D. Tollefsen and S. E. Dosso, "Bayesian geoacoustic inversion of ship noise on a horizontal array," J. Acoust. Soc. Am. **124**, 788–795 (2008).
[41]P. Gerstoft and D. F. Gingras, "Parameter estimation using multifrequency range-dependent acoustic data in shallow water," J. Acoust. Soc. Am. **99**, 2839–2850 (1996).
[42]D. Jackson and M. Richardson, *High-Frequency Seafloor Acoustics* (Springer, New York, 2010), pp. 123–151.